Eur. Phys. J. D **19**, 275–291 (2002)
DOI: 10.1140/epjd/e20020096

THE EUROPEAN PHYSICAL JOURNAL D
EDP Sciences

A spectroscopic investigation of $Y_3Al_5O_{12}$:Pr^{3+} in translucent ceramic form: Crystal field analysis assisted by configuration-interaction

O.K. Moune[1], Y. Rabinovitch[1], D. Tétard[2], M. Pham-Thi[3], E. Lallier[3], and M.D. Faucher[1,a]

[1] Structures, Propriétés et Modélisation des Solides[b], École Centrale Paris, 92295 Châtenay-Malabry Cedex, France
[2] Science des Procédés Céramiques et de Traitements de Surfaces[c], Faculté des Sciences de Limoges, 123 avenue Albert Thomas, 87060 Limoges Cedex, France
[3] THALES, Research & Technology, domaine de Corbeville, 91404 Orsay Cedex, France

Received 9 November 2001 and Received in final form 8 February 2002

Abstract. This paper presents an investigation of Pr^{3+} doped in the D_2 site of $Y_3Al_5O_{12}$ (YAG), for the first time on a translucent ceramic sample free of spurious phases, impurity or pair sites. The optical study is carried out by optical absorption, excitation, and emission by selective excitation into $^1D_2$ and $^3P_0$, at different temperatures between 20 K and 60 K, in the 4 300–23 000 cm^{-1} range. A detailed account of the line assignments is given. 67 over 91 levels of the $4f^2$ configuration are determined. Several crystal field calculations within the ground configuration $4f^2$ and the larger matrix $4f^2 + 4f6p$ are carried out. The energy level fit is slightly improved by configuration interaction. The $^3P_2$ and $^1I_6$ levels are strongly mixed together by the large 6th order crystal field parameters. In sintered samples with different Pr^{3+} concentrations, satellite lines with intensities increasing quadratically with the concentration are observed. A few weak lines forbidden in D_2 site symmetry are observed.

PACS. 71.70.Ch Crystal and ligand fields – 78.20.-e Optical properties of bulk materials and thin films – 42.70.-a Optical materials

1 Introduction

Yttrium aluminium garnet $Y_3Al_5O_{12}$ (YAG) is a stable refractory material with remarkable mechanical properties and a high thermal conductivity. It resists to high temperatures and thermal choc. It is transparent over a wide spectral range which makes it a privileged host for luminescent applications [1]. Rare-earth doped $Y_3Al_5O_{12}$ is studied in connection with a score of applications: solid state lasers (Nd^{3+}, Ho^{3+}, Er^{3+}, Tm^{3+}, Yb^{3+}), fluorescent lighting, field emission display, and plasma flat panel display devices, the most widely studied being the neodymium doped compound. Pr^{3+} doped $Y_3Al_5O_{12}$ was been investigated as a potential amplifying medium at 1.3 μm (the $^1G_4 \rightarrow {}^3H_4$ transition) [2], a wavelength of interest in optical communications.

There exist a small number of papers devoted to the analysis of the $4f^2$ spectrum of YAG: Pr^{3+} and the determination of the energy level scheme [3–6]. Some levels have been determined by two-photon absorption [7]. Lifetimes and the IR-to-blue up-conversion in YAG–Pr^{3+} have been reported by Malta *et al.* [8]. The problems connected with the interpretations of the experimental observations have not all been completely solved. The optical investigations are hampered by a score of spurious lines, the origin of which is obscure. This occurs, not only for the praseodymium but also for the neodymium and the thulium doped compound. This might be connected to the fact that other phases than YAG are likely to coexist in the samples. Goldschmidt *et al.* [9] derived from the values of the ionic radii, the expression of a tolerance factor for the formation of the perovskite structure. The experimentally determined lower limit is equal to 0.84 in the $Ln_2O_3{\cdot}Al_2O_3$ system. It is equal to 0.88 for the $Y_2O_3{\cdot}Al_2O_3$ combination. Schneider, Roth and Waring [10] have shown that $Y_3Al_5O_{12}$ lies just within a small zone of compositions where both the garnet $Y_3Al_5O_{12}$ and the perovskite $YAlO_3$ can coexist. Indeed, for small deviations from stoechiometry, or for low sintering temperatures, $YAlO_3$ and $Y_4Al_2O_9$ are detected in the X-ray patterns. However, the interpretation of the spectra meets with problems, even in stoechiometric compounds. It may be connected with the ability for a certain amount of rare earth ion to occupy the the Al^{3+} site [11] or with the fact that at a microscopic scale, there are strains leading to different local arrangements. Some authors assume that

[a] e-mail: faucher@spms.ecp.fr
[b] UMR 8580 du CNRS
[c] UMR 6638 du CNRS

these local arrangements are minority sites [6]. Tiseanu *et al.* [12] ascribe the origin of satellite lines in YAG:Tm^{3+} to non stoichiometric defects, Tm^{3+} in octahedral sites or pairs. This last hypothesis is supported by Guillot-Noël *et al.* [13] for the case of YAG:Nd^{3+}. A strong electron-phonon coupling has been observed for some transitions of YAG:Tm^{3+} [12].

Some discrepancies between the earlier results of different authors have prompted us to reinvestigate the position and assignment of the energy levels of Pr^{3+} doped YAG.

In Sections 2 and 3 will be given some details on the experimental investigation which consists in a combination of absorption measurements, site selective and time resolved excitation and emission. Since the samples morphology and composition are of paramount importance, a special care was brought to their high temperature synthesis and also to the selection of the levels pertaining to the Pr^{3+} site in the YAG structure. In Section 4 the crystal field analysis will be discussed.

2 Synthesis and structure

YAG:Pr^{3+} in polycrystalline powder form was prepared by sintering for several hours a stoichiometric mixture of Al_2O_3, Y_2O_3, and of Pr_2O_3 above 1 700 °C in vacuum [14]. Three samples with concentrations equal to 1, 0.2, and 0.07 at.% based on Y^{3+}, were synthetized. One problem consists in the extreme ability for the formation of the two concurrent phases $YAlO_3$ and $Y_4Al_2O_9$ which are both richer than YAG in yttrium. The 1% sample was molten at the contact with the alumina crucible so that the alumina excess prevented the formation of the two other phases and the totality of yttrium and praseodymium was in the garnet phase. The alumina excess did not impede the spectroscopic investigation since no praseodymium entered in that compound. The 0.2% sample also stuck to the alumina crucible and was nearly free of spurious phases. The 0.07% sample, prepared with additional SiO_2, was translucent and revealed no spurious phase [14]. Optical absorption measurements were more sensitive than X-ray analyses to check the purity of the YAG phase. The results of a microprobe analysis of our 0.07% Pr^{3+} doped sample are the following: on a total of 100 atoms (yttrium + praseodymium, aluminium, oxygen) there are 13.79 and 25.75 atomic % yttrium and aluminium respectively. There exists in the final sample a 0.75% Al^{3+} excess and a 1.21% Y^{3+} deficiency with respect to the theoretical composition. The X-ray diffraction pattern reveals no Al_2O_3 lines.

The overall crystal structure of yttrium aluminium garnet is cubic. It belongs to the O_h^{10} ($Ia3d$) space group [15,16]. There are eight equivalent yttrium sites per elementary unit cell. Their site symmetry is D_2, the three twofold axes being along the (100), (110) and (1$\bar{1}$0) directions. The cation-anion distances are equal to 2.432 and 2.303, 1.937 and 1.761 Å for the (c) dodecahedral (Y^{3+}), (a) octahedral (Al^{3+}) and (d) tetrahedral (Al^{3+}) sites respectively.

The four nondegenerate irreducible representations of Pr^{3+} substituting for Y^{3+} in the D_2 point group are Γ_1, Γ_2, Γ_3 and Γ_4. In this site symmetry, the degeneracy of the SLJM levels is completely removed by the crystal field and each multiplet is split into $2J+1$ components. The selection rule for the electric dipole transitions is just $\Gamma_i \neq \Gamma_f$ which states that transitions between identical representations are forbidden.

3 Spectroscopic measurements

The absorption spectra of the three samples in the 440 to 2 400 nm spectral area were recorded by a CARY 5E spectrometer. The sample temperature could be varied between 20 and 60 K by the means of a He closed cycle cryostat (model CP-62-ST/5 from Cryophysics).

The emission and excitation spectra of the 0.07 at.% sample in the 430–860 nm spectral region were obtained by means of an optical parametric oscillator (Quanta-Ray MOPO-730) pumped by the third harmonic at 355 nm (8 ns pulse at 10 Hz, 0.1 cm^{-1} width) of a Q-switched neodymium YAG laser (GCR-230) from Spectra-Physics. They were recorded using a double grating spectrometer (model PHO from Coderg) equipped with a R928 Hamamatsu photomultiplier. Time-resolved fluorescence and fluorescence lifetimes were recorded *via* a digital oscilloscope (Tektronix 2430) coupled with a micro computer (Ref. [17]). The selective excitations into $^1D_2$ and $^3P_0$ were achieved by tuning the excitation frequency in resonance with the $^1D_2(2)$, and $^3P_0$ levels, and the excitation spectra by monitoring emissions from $^1D_2$ and $^3P_0$.

3.1 Satellite lines. Influence of the concentration of Pr^{3+} ions

Detailed absorption spectra at 20 K in the $^3H_4(1) \rightarrow {}^3P_0$ area are shown in Figure 1. They refer to three samples with different Pr^{3+} concentrations (1, 0.2, and 0.07 at.%). As pointed out higher we made sure that they were free of spurious phases containing praseodymium. Yet the spectrum of the 1% doped sample is extremely intricate and contains several strong lines.

The presence of satellite lines in the spectra of rare earth doped YAG, which was pointed out earlier [3–6,11, 18–20], has on some occasions prevented the determination of complete energy level schemes. Many authors explain the growth of satellites by the existence of rare earth pairs. For instance, Lupei *et al.* [11] interpret the concentration dependent satellite lines observed in YAG:Nd^{3+} by pairs created by neighbours placed on one of the 14 sites of the first, second and third cationic coordination sphere: 4 at 3.68 Å, 8 at 5.62 Å and 2 at 6.00 Å. Guillot-Noël *et al.*, investigating Nd^{3+} ions in a YVO_4 single crystal by optical spectroscopy and electron paramagnetic resonance (EPR) [18] observe concentration dependent satellites on each side of the two bands in the $^4I_{9/2} \rightarrow {}^4F_{3/2}$ absorption spectra at relatively low concentration (0.58%). No satellites are present however, neither in the absorption

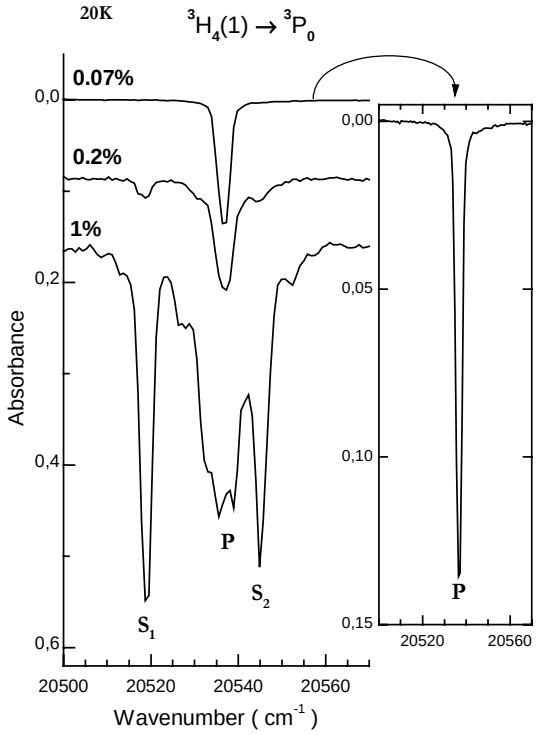

Fig. 1. $^3H_4 \rightarrow {}^3P_0$ absorption spectra at 20 K with different Pr^{3+} concentrations in YAG: 0.07%, 0.2% and 1%. *P*: Principal line, S_1, S_2: satellite lines.

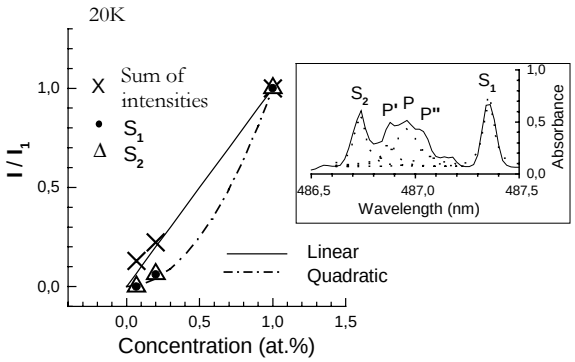

Fig. 2. Variation at 20 K of the normalized (divided by the value for 1%) total intensity of the $^3H_4(1) \rightarrow {}^3P_0$ transition, of S_1 and S_2, with the concentration of the Pr^{3+} ion. Insert: deconvolution of the spectral lines.

spectrum nor in the EPR spectrum at low concentration (0.05%) in this host. The satellites are interpreted as produced by Nd^{3+}–Nd^{3+} pairs coupled by magnetic dipolar interaction. The quadratical concentration dependence of the intensity of some Pr^{3+} absorption lines in LaF_3 (3%, 5%, 7%) is also related to ion pairs [19].

Other authors argue in favor of rare earths placed in different sites. Gruber *et al.* [6] assume that different sites arise from defects caused by loss of oxygen from the lattice during crystal growth and exclude the possibility of formation of pair or clusters of Pr^{3+} ions, because the weak peaks retain their relative intensities at two different concentrations (0.02 and 0.08 at.%). Malinowski *et al.* [20] report 7 peaks for $^3H_4(1) \rightarrow {}^1D_2(1,2)$ instead of 2 expected lines in the excitation spectra of the $^1D_2 \rightarrow {}^3H_6$ fluorescence of 0.08 at.% Pr^{3+} doped YAG single crystal. These authors suggest that the crystal field and atomic parameters can be weakly modified by the presence of a second Pr^{3+} ion substituted to a near neighbor Y^{3+} in a regular D_2 site and detect 6 non-equivalent sites. They also evoke also the possibility of Pr^{3+} entering in the a sites of Al^{3+}. Antic-Fidancev *et al.* [5] show by selective excitation that each excitation corresponds to one different satellite line. These authors suggest an electron-phonon interaction of the ground state level.

This short survey shows that there is no uniquely accepted interpretation of the satellite lines in rare earth doped YAG.

In Figure 1 the absorption spectra become progressively cleaner as the Pr^{3+} concentration decreases and finally for a dilute concentration (0.07 at.%), the presence of only one expected line at 20 536 cm^{-1} indicates that the Pr^{3+} ions occupy one site symmetry. We shall refer to this line as *P*. It corresponds to the $^3H_4(1) \rightarrow {}^3P_0$ transition produced by Pr^{3+} ions in the D_2 symmetry of the undistorted site of Y^{3+}. A close examination reveals no other lines around *P* in the 0.07% sample (see inset of Fig. 1). Gruber *et al.* [6] investigating a Czochralsky grown crystal weakly doped with Pr^{3+} (0.08%) detect 4 weak lines close to the strong one at 20 534 cm^{-1} (Fig. 6 in Ref. [6]). The positions of two of these lines match those of two satellites S_1 and S_2 at 20 519 and 20 545 cm^{-1} respectively, appearing in our 0.2 at.% sample, on each side of *P*. For the more concentrated sample, (1 at.%), these satellites have grown as high as the central massif containing, in addition to *P*, two shoulders (P' and P''), one of which is the satellite observed by Gruber *et al.* 4 cm^{-1} to higher energies from *P*. A deconvolution of the spectrum yields intensities proportional to 52, 27, 78, 18 and 64 for S_2, P', *P*, P'' and S_1 respectively (insert Fig. 2). The total intensity of the $^3H_4(1) \rightarrow {}^3P_0$ transition is distributed between these five components and the percentage of Pr^{3+} ions occupying isolated sites in the theoretical D_2 environment (site *P*) is no more than 33%. Figure 2 shows the variation of the total intensities of the $^3H_4(1) \rightarrow {}^3P_0$ transition on one hand, of S_1 and S_2 on the other. The total intensity of the $^3H_4(1) \rightarrow {}^3P_0$ transition varies linearly with the concentration while the variations of S_1 and S_2 with the concentration are very similar and quasi quadratic. This variation is clearly connected with the progressive approach of other rare earth ions.

The probability for two doping ions to be found in a given volume is approximately proportional to the total number of available sites in that volume multiplied by the square of the concentration of doping ions. A detailed account of occurrence probabilities in doped crystals is given by Lupei *et al.* in reference [11]. There are 14 Y^{3+} sites available in a 6 Å sphere around one Pr^{3+}. The probability for the existence of a pair in this volume is roughly equal to $14C^2$ which parallels the experimentally stated variation. However, the C^2 variation of the satellites intensity says nothing about the physical interaction

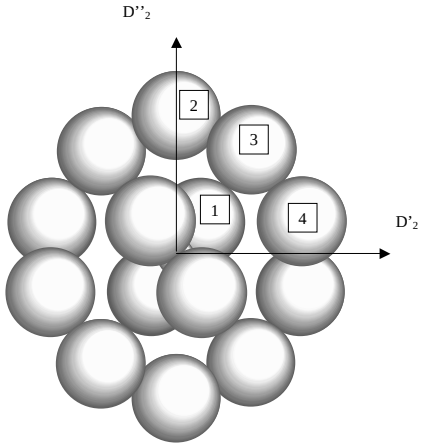

Fig. 3. First, second and third shell of Y^{3*} neighbours in $Y_3Al_5O_{12}$. The atomic radii have been increased out of proportions in order to show clearly the symmetry operations: D_2 around the axis perpendicular to the figure, D'_2 and D''_2 at right angles in the plane. Atom 1 is in the first shell at 3.68 Å, atom 2 at 6.00 Å, atoms 3 and 4 at 5.62 Å.

mechanism. Figure 3 shows that it is possible, given the $3D_2$ operations of the site symmetry group, to define among the 14 closest rare-earth neighbours, four non-equivalent substitutions leading to slightly different symmetry sites for the central ion: one in the first shell of Y^{3+} nearest neighbours, and three in the second shell at 5.62 and 6.00 Å. A crude evaluation of the perturbation created by a Pr^{3+} ion in the first shell at 3.68 Å on the crystal field parameters of a Pr^{3+} ion with oxygens first neighbours was performed by utilizing the covalo-electrostatic model. The electrostatic contribution was assumed to be the same with and without second neighbours. The crystal field parameters decreased, by 5, 10 and 20% for the second, fourth and sixth order parameters respectively. The change of the free ion parameters was not evaluated. Crystal field calculations with modified parameters show that the $^3H_4(3)-{}^3H_4(1)$ and $^3H_4(9)-{}^3H_4(1)$ splittings are reduced by 9 and 65 cm^{-1} respectively by the presence of the substituted Pr^{3+}. We are therefore inclined to assign the most remote satellite at 20 519 cm^{-1} to a Pr^{3+} ion on the first coordination sphere at 3.68 Å from the central ion, and the other satellite at 20 545 cm^{-1} (in addition to those eventually nearly coincident with P), to a Pr^{3+} ion substituted on the second coordination shell. Other Pr^{3+} eventually located on farther sites (there are 8 more available sites at 6.61 Å and 4 at 7.04 Å) contribute to the inhomogeneous broadening of the central line P.

The intensity of the absorption lines is proportional to C and the probability for the occurrence of pairs to $14C^2$, hence for a 1% concentration, the intensity of the satellite lines should be grossly $14C^2/C = 0.14$ times that of the $^3H_4(1) \rightarrow {}^3P_0$ transition. The above considerations show that the sum of the experimentally measured satellite intensities $S_1 + S_2 + P' + P''$ represents 67% of the total transition. If we assume that the satellite lines have all the same transition probabilities, the sum of their intensities is more than 4 times larger than expected. The large difference between the atomic radii of Y^{3+} and Pr^{3+} probably destroys the statistical distribution of Pr^{3+} in the matrix and there exists in the samples a tendency for a crowding of Pr^{3+} ions in distorted zones, perhaps close to the surface of the grains.

In addition to satellites which appear in the vicinity of the $^3H_4(1) \rightarrow {}^3P_0$ absorption line, similar kinds of satellites and concentration dependences are observed in the $^3H_4(1) \rightarrow {}^1D_2$, $^3P_1$, $^1I_6$ absorption spectra of the samples with 0.2 and 1 at.% concentrations. Since no satellite lines are observed in the absorption spectra of the 0.07 at.% doped sample (except a broad band at about 16 430 cm^{-1}), the energy levels of Pr^{3+} ion were determined from the measurements on this sample and all the absorption and emission spectra analysed hereafter refer to it. It is assumed that for this concentration (0.07 at.% Pr^{3+}), and within the detection limits of of our experimental setup, all the Pr^{3+} ions introduced in the matrix occupy the D_2 site only.

The several perturbed minority sites reported in the earlier works: Hooge −5 at.% [3], Gourley −1 at.% [4], Antic-Fidancev *et al.* −1 at.% [5] concerning Pr^{3+} doped YAG arise therefore from a too high concentration of Pr^{3+} ions.

Gruber *et al.* [6] as well as Malinowski *et al.* [7] analysed the optical spectra of 0.08 and 0.02 at.% doped single crystal, with a concentration similar to our lowest one. Yet they always observed additional lines in addition to the main one. The absence of spurious lines in our sample is due, not only to the low concentration, but also to the synthesis method [14].

3.2 Optical investigation: determination of the position and representation of the energy levels

The average values of the three lowest levels of $^3H_4$ multiplet observed by us are 0, 18 and 50 cm^{-1}. In the absorption spectra, the transitions from the two and three lowest levels of $^3H_4(1,2,3)$ to the higher excited levels of $^3H_6$, $^3F_{2,3,4}$, $^1G_4$, $^1D_2$, $^3P_{0,1,2}$, $^1I_6$ multiplets were recorded at 20 and 60 K respectively. At 20 K the two lowest levels of $^3H_4$ are thermally populated and at 60 K the three lowest ones. The *ab initio* calculation based on the crystal structure gives Γ_3, Γ_1 and Γ_4 for the irreducible representations of $^3H_4(1,2,3)$, as discussed in Section 4. The variation of the relative intensities of the absorption lines at 20 and 60 K permitted us to determine which starting and terminal levels are involved for each absorption line. In Figure 4, the absorption spectrum corresponding to the $^3H_4(1,2,3) \rightarrow {}^1D_2$ transitions at 20 K and 60 K is shown. We can see clearly that lines 1 and 2 correspond to $^3H_4(3) \rightarrow {}^1D_2(1,2)$, line 3 to $^3H_4(2) \rightarrow {}^1D_2(2)$, lines 4 and 5 to $^3H_4(1) \rightarrow {}^1D_2(1,2)$, line 6 to $^3H_4(3) \rightarrow {}^1D_2(3)$, line 7 to $^3H_4(1) \rightarrow {}^1D_2(3)$, line 8 to $^3H_4(3) \rightarrow {}^1D_2(4)$, line 9 $^3H_4(2) \rightarrow {}^1D_2(4)$ (more visible for the 0.2% sample) and line 10 to $^3H_4(1) \rightarrow {}^1D_2(5)$. The position of 5 sublevels of $^1D_2$ multiplet are thus determined as: 16 403, 16 413, 16 684, 17 082, 17 215 cm^{-1}. $^1D_2(2)$ (line 5) is associated with two temperature induced lines (lines 3 and 2)

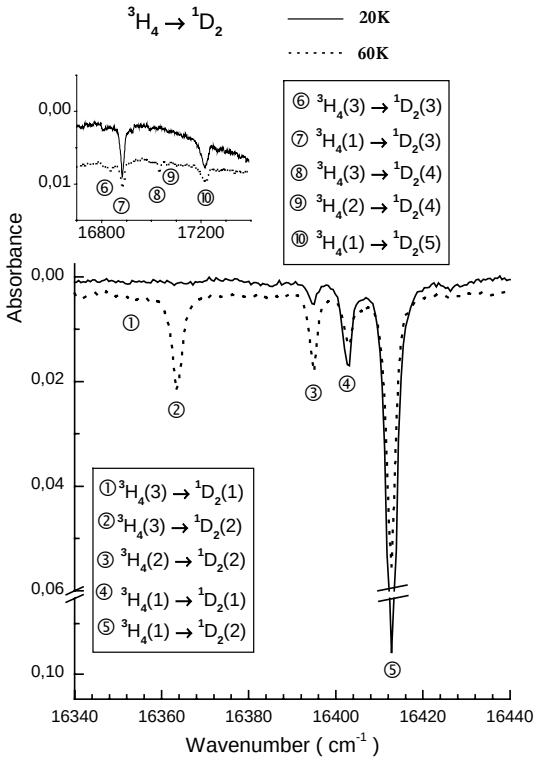

Fig. 4. $^3H_4 \rightarrow {}^1D_2$ absorption spectrum at 20 K (solid line) and at 60 K (dotted line).

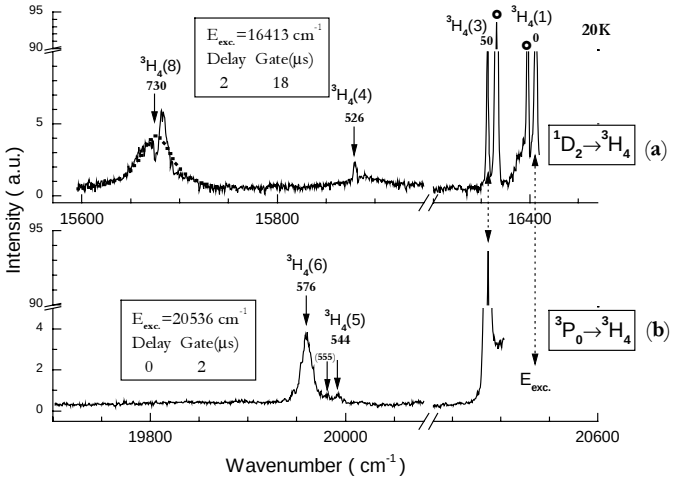

Fig. 5. $^1D_2 \rightarrow {}^3H_4$ (a) and $^3P_0 \rightarrow {}^3H_4$ (b) emission spectrum at 20 K: (a) under selective excitation into 16 413 cm^{-1}, (b) under selective excitation into 20 536 cm^{-1}. Dotted double and single solid arrows show the positions of the $^3H_4$ sub-levels which are observed in both emission spectra and in one of the two emission spectra, respectively. (o) indicates emission lines from $^1D_2(2)$.

separated by 18 and 49 cm^{-1} which assigns its symmetry label as Γ_2. $^1D_2(1)$ level (line 4) is associated with one hot line (line 1) separated by 50 cm^{-1} and its symmetry label is Γ_1 or Γ_2. The fact that the $^1D_2$ multiplet ($J = 2$) has only one Γ_2 indicates that $^1D_2(1)$ is Γ_1. $^1D_2(3)$ (line 7) is associated with one hot line (line 6) separated by 50 cm^{-1} and $^1D_2(4)$ is deduced from two temperature induced lines (lines 8 and 9) separated by 33 cm^{-1}. No hot line seems associated with $^1D_2(5)$ (line 10). The representations of the $^1D_2$ multiplet are therefore determined from the absorption spectrum as the following: 16 403Γ_1, 16 413Γ_2, 16 884Γ_1, 17 082Γ_3, 171 215Γ_4. The position of these energy levels determined by us are slightly different from the values of the authors of reference [6], but our symmetry assignments are in agreement with theirs.

The position and symmetry assignments of the energy levels were analyzed by the means of four kinds of optical spectra:

1- absorption from to $^3H_4(1,2,3)$,
2- emission from $^3P_0$,
3- emission from $^1D_2(1,2)$,
4- excitation monitoring emissions from $^1D_2(1)$ or $^3P_0$.

The levels of $^3H_{4,6}$ were determined from 1-2-3, $^3H_5$ from 2-3, $^3F_{2-4}$ from 1-2, $^1G_4$ from 1, $^1D_2$, $^3P_{0-2}$, and $^1I_6$ from 1 and 4.

In the absorption and emission spectra, all the allowed transitions are not necessarily observed, since their transition probabilities may be very small. The fact that only the transitions between identical representations are forbidden and that allowed transitions may be weak, makes the assignment of irreducible representation difficult or impossible for many levels, from experimental considerations only.

Table 1 shows the possible combinations which can be made with the informations given by the absorption and emission spectra. The representations authorized in absorption are listed in column Γ_a, the transitions authorized in emission from $^3P_0$ and $^1D_2(1)$ in column Γ_b, from $^1D_2(2)$ in Γ_c. Γ_{ab}, Γ_{bc} and Γ_{abc} indicate finally the possible representations determined by the combination of these events.

From the absorption spectra, only Γ_2 can be assigned: if at 60 K the transitions from the three lowest levels of $^3H_4$ to a terminal level are observed, then the only possible representation of this terminal level is Γ_2. 7 levels are assigned as Γ_2. The other observed levels have two or three possibles representations depending on the number and the nature of the hot lines associated.

The symmetry labels of the energy levels observed from selective excitation into $^3P_0$ are Γ_2, Γ_3, or Γ_4. From selective excitation into this level (Figs. 5, 7–10), some additional energy levels are determined and restricts the possible representations assigned from absorption spectra.

From the selective excitation into $^1D_2(2)$ Γ_2 at 16 413 cm^{-1} (Fig. 6), the emission lines from both $^1D_2(1,2)$ are observed at 20 K. $^1D_2(1,2)$ are separated by 10 cm^{-1} only and $^1D_2(2)$ is thermally populated at 20 K. In the same way as for the absorption lines from $^3H_4(1,2)$, the variations of the relative intensities of the emission lines between 20 and 60 K determines from which level the emissions take place. In Figure 6, lines 2 and 3 correspond to the emissions $^1D_2(2)\Gamma_2 \rightarrow {}^3H_4(2,3)$ and lines 1, 4, 5 and 6 correspond to $^1D_2(1)\Gamma_1 \rightarrow {}^3H_4(1,3,4,8)$.

Line 6 shows a dip at 15 673 cm^{-1} which seems to define two transitions. Actually, it is interpreted as an

Table 1. Determination of the possible symmetry labels of the energy levels based on the observed absorption and emission spectra.

Absorption			Emission							
$^3H_4(1)$	$^3H_4(2)$	$^3H_4(3)$	Γ_a	$^3P_0$	Γ_b	$^1D_2(1)$	Γ_c	Γ_{ab}	Γ_{bc}	Γ_{abc}
Γ_3	Γ_1	Γ_4		$^1D_2(1)$		Γ_2				
				Γ_1						
x	x	x	2					2	2	2
x	x	-	2, 4	x	2, 3, 4	x	1, 3, 4	2, 4	3, 4	4
			2, 4	x	2, 3, 4	-	1, 2, 3, 4		2, 3, 4	2, 4
			2, 4	-	1, 2, 3, 4	x	1, 2, 3	2, 4	1, 3, 4	4
			2, 4	-	1, 2, 3, 4	-	1, 2, 3, 4		1, 2, 3, 4	2, 4
x	-	x	1, 2	x	2, 3, 4	x	1, 3, 4	2		-
			1, 2	x	2, 3, 4	-	1, 2, 3, 4			2
			1, 2	-	1, 2, 3, 4	x	1, 3, 4	1, 2		1
			1, 2	-	1, 2, 3, 4	-	1, 2, 3, 4			1, 2
-	x	x	2, 3	x	2, 3, 4	x	1, 3, 4	2, 3		3
			2, 3	x	2, 3, 4	-	1, 2, 3, 4			2, 3
			2, 3	-	1, 2, 3, 4	x	1, 3, 4	2, 3		3
			2, 3	-	1, 2, 3, 4	-	1, 2, 3, 4			2, 3
x	-	-	1, 2, 4	x	2, 3, 4	x	1, 3, 4	2, 4		4
			1, 2, 4	x	2, 3, 4	-	1, 2, 3, 4			2, 4
			1, 2, 4	-	1, 2, 3, 4	x	1, 3, 4	1, 2, 4		1, 4
			1, 2, 4	-	1, 2, 3, 4	-	1, 2, 3, 4			1, 2, 4
-	x	-	2, 3, 4	x	2, 3, 4	x	1, 3, 4	2, 3, 4		3, 4
			2, 3, 4	x	2, 3, 4	-	1, 2, 3, 4			2, 3, 4
			2, 3, 4	-	1, 2, 3, 4	x	1, 3, 4	2, 3, 4		3, 4
			2, 3, 4	-	1, 2, 3, 4	-	1, 2, 3, 4			2, 3, 4
-	-	x	1, 2, 3	x	2, 3, 4	x	1, 3, 4	2, 3		3
			1, 2, 3	x	2, 3, 4	-	1, 2, 3, 4			2, 3
			1, 2, 3	-	1, 2, 3, 4	x	1, 3, 4	1, 2, 3		3
			1, 2, 3	-	1, 2, 3, 4	-	1, 2, 3, 4			1, 2, 3
-	-	-	1, 2, 3, 4	x	2, 3, 4	x	1, 3, 4	2, 3, 4		3, 4
				x	2, 3, 4	-	1, 2, 3, 4	2, 3, 4		2, 3, 4
				-	1, 2, 3, 4	x	1, 3, 4	1, 2, 3, 4		1, 3, 4

x : transition is observed, - : transition is not observed, Γ_a: label based on the absorption spectrum from $^3H_4(1,2,3)$; Γ_b: label based on the emission spectrum from $^3P_0$ or $^1D_2(1)$; Γ_c: label based on the emission spectrum from $^1D_2(2)$; Γ_{ab}: label based on the absorption and emission spectra from $^3P_0$ or $^1D_2(1)$; Γ_{bc}: label based on the emission spectra from $^3P_0$ and $^1D_2(1,2)$; Γ_{abc}: label based on the absorption and emission spectra from $^3P_0$ and $^1D_2(1,2)$.

excited state absorption from $^3F_3(2)$ (populated by $^3F_3(1)$) up to $^3P_2(2)$. The mechanism would be:

$$^1D_2(1)\ (16\,403) \rightarrow {}^3H_4(8)\ (730) + 15\,673\ \text{cm}^{-1},$$
$$^3F_3(2)\ (6\,499) + 15\,673\ \text{cm}^{-1} \rightarrow 22\,172\ \text{cm}^{-1}.$$

The energy mismatch with respect to $^3P_2(2)$ is equal to 20 cm^{-1}. In Figure 6, the assumed shape of line 6 is drawn by a bold line.

Three cases arise in the selective excitation into $^1D_2(2)$: emission from $^1D_2(1)\Gamma_1$ only, from $^1D_2(2)\Gamma_2$, and from $^1D_2(1,2)$. In the first case, the symmetry label of the terminal level is Γ_2, Γ_3, or Γ_4, for the second case, Γ_1, Γ_3, or Γ_4 and for the last one Γ_3 or Γ_4. In this way, the selective excitation into $^1D_2(2)$ at 20 K and 60 K allows to determine some more energy levels of $^3H_{4,5,6}$ and $^3F_{2,3,4}$ and to restrict the possible representations assigned from absorption and emission spectra from the $^3P_0$ level.

The excitation spectra obtained by monitoring the $^1D_2(1) \rightarrow {}^3H_6(1)$ emission at 12 101 cm^{-1} while the excitation wavelength is scanned through $^3H_4(1) \rightarrow {}^1D_2$ are the same as the absorption spectra. The excitation spectra obtained by monitoring the $^3P_0 \rightarrow {}^3F_3(3)$ emission at 13 975 cm^{-1} while the excitation wavelength is scanned through $^3H_4 \rightarrow {}^3P_{0,1}$, $^1I_6$, $^3P_2$, contains two more $^1I_6$ levels (at 20 728 and 20 746 cm^{-1}) than the absorption spectrum. Figures 11 and 12 show the absorption and excitation spectra at 60 K. In the excitation spectra, the lines marked with solid arrows, open and solid circles indicate absorption from $^3H_4(1)$, $^3H_4(2)$ and from $^3H_4(3)$,

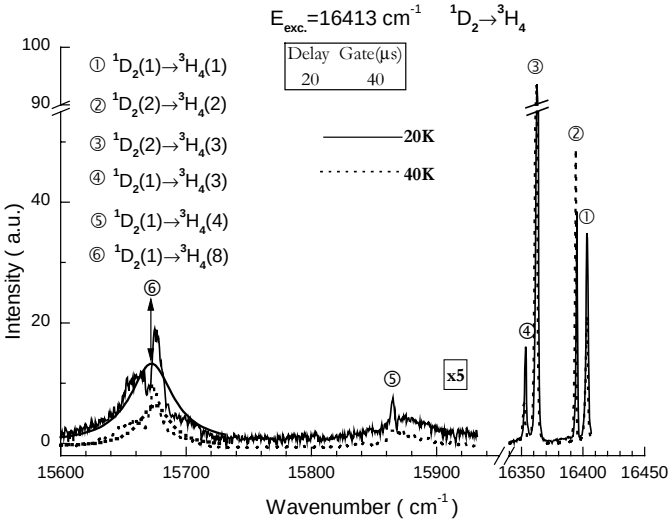

Fig. 6. $^1D_2 \rightarrow {}^3H_4$ emission spectrum at 20 K (solid line) and at 60 K (dotted line) upon selective excitation into $^1D_2(2)$ at 16 413 cm^{-1}.

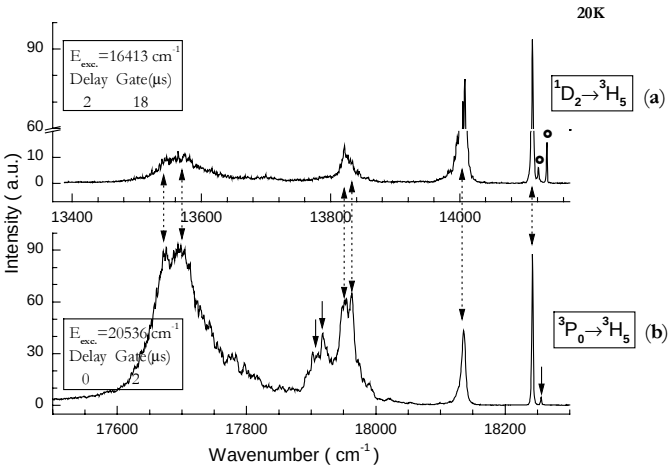

Fig. 7. $^1D_2 \rightarrow {}^3H_5$ (a) and $^3P_0 \rightarrow {}^3H_5$ (b) emission spectrum at 20 K: (a) under selective excitation into 16 413 cm^{-1}, (b) under selective excitation into 20 536 cm^{-1}. Dotted double and single solid arrows show the positions of the $^3H_5$ sub-levels which are observed in both emission spectra and in one of the two emission spectra, respectively; (o) indicates emission lines from $^1D_2(2)$.

respectively. The lines marked with dotted arrows indicate the position of energy levels deduced from the hot lines.

The results are given in Tables 2 and 3 which list the 69 experimental levels observed by absorption from $^3H_4$ or by emission from $^3P_0$, $^1D_2$ and which belong to Pr^{3+} in the dodecahedral site of the YAG matrix. Their possible assignments are indicated in the last column. The lifetimes of the $^3P_0$ and $^1D_2$ levels have been measured. At 20 K, they are equal to 11 and 262 μs, respectively.

The assignment is unique for 21 of these levels (6, 7, 4 and 4 levels identified as Γ_1, Γ_2, Γ_3 and Γ_4 respectively). For another 20, there are two possibilities: 3 (Γ_3 or Γ_4), 8 (Γ_2 or Γ_4), 4 (Γ_1 or Γ_2), 1 (Γ_1 or Γ_4) and 4 (Γ_2, Γ_3)), and for 28, there are three possibilities; 17 can be (Γ_2, Γ_3 or

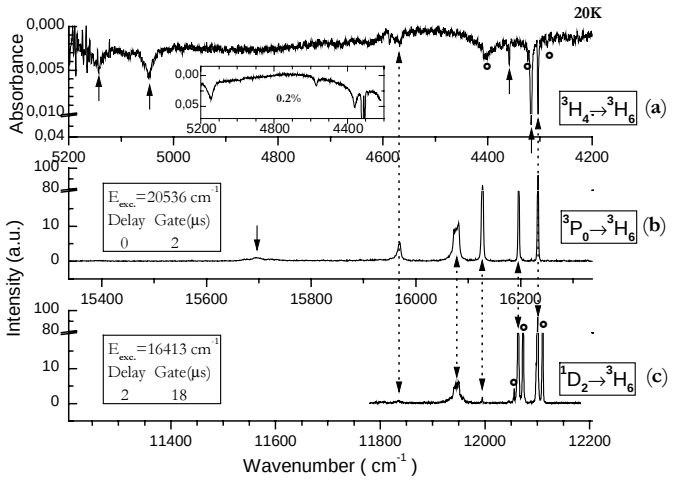

Fig. 8. $^3H_4 \rightarrow {}^3H_6$ absorption (a), $^3P_0 \rightarrow {}^3H_6$ (b) and $^1D_2 \rightarrow {}^3H_6$ (c) emission spectra at 20 K; (o) indicates absorption lines from $^3H_4(2)$ (a) and emission lines from $^1D_2(2)$ (c).

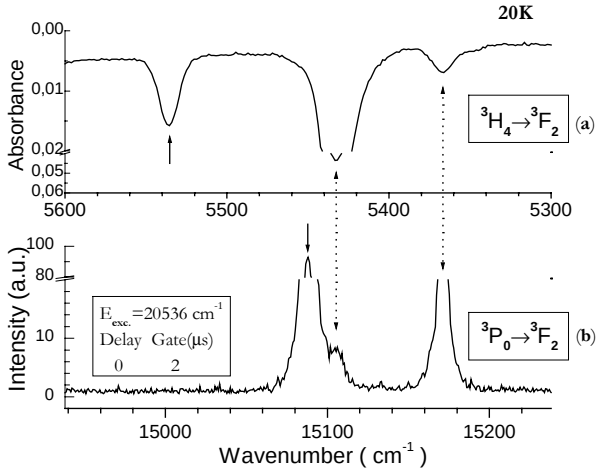

Fig. 9. $^3H_4 \rightarrow {}^3F_2$ absorption (a), $^3P_0 \rightarrow {}^3F_2$ (b) emission spectrum at 20 K. The arrows have the same meaning as in Figure 7.

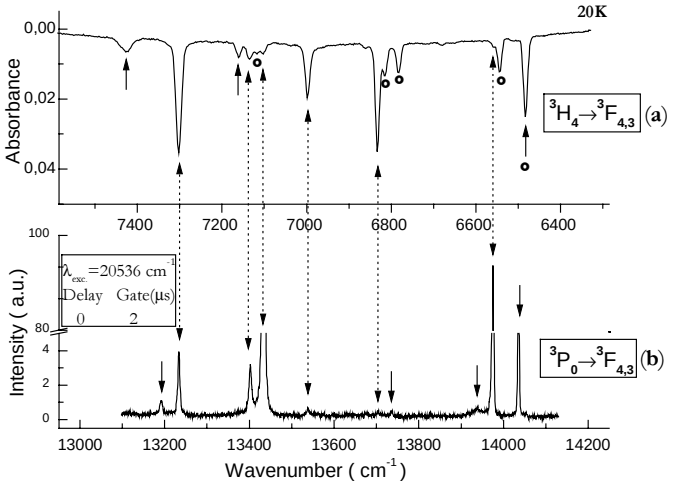

Fig. 10. $^3H_4 \rightarrow {}^3F_{4,3}$ absorption (a), $^3P_0 \rightarrow {}^3F_{4,3}$ (b) emission spectrum at 20 K. The arrows have the same meaning as in Figure 7; (o) indicates absorption line from $^3H_4(2)$.

Table 2. Absorption spectrum at 60 K and emission at 20 K from $^3P_0$ and $^1D_2(1,2)$ (cm^{-1}).

Absorption			Emission			Terminal level $^{2S+1}L_J$		Γ_n
			$E_{exc} = 20\,536$ cm^{-1}		$E_{exc} = 16\,413$ cm^{-1}			
Starting level			Starting level					
$^3H_4(1)$	$^3H_4(2)$	$^3H_4(3)$	$^3P_0$	$^1D_2(1)$	$^1D_2(2)$			
0 Γ_3	18 Γ_1	50 Γ_4	20 536 Γ_1	16 403 Γ_1	16 413 Γ_2			
				16 403		0	$^3H_4$	3
					16 395	18		1
			20 485	16 353	16 363	50		4
				15 877		526		2, 3, 4
			19 992 vw			544		2, 3, 4
			19 981 vw			(555)		2, 3, 4
			19 960			576		2, 3, 4
				15 673		730		2, 3, 4
			18 256		14 135	2 279	$^3H_5$	3, 4
			18 243	14 112	14 112	2 293		3, 4
			18 136	14 408		2 398		2, 3, 4
			17 962	13 832 sh		2 574		2, 3, 4
			17 952	13 821		2 583		3, 4
			17 918			2 618		2, 3, 4
			17 907 sh			(2 629)		2, 3, 4
			17 697	13 573[a]		2 839		2, 3, 4
			17 675	13 545[a]		2 861		2, 3, 4
4 303	4 285		16 234	12 101	12 111	4 303	$^3H_6$	4
4 316		4 266		12 087 b	12 098	4 316		1
	4 322	4 290	16 197	12 063	12 073	4 340		3
4 358				12 046 b	12 056	4 358		1, 4
	4 402 b		16 127	11 995		4 409		2, **3**, **4**
			16 078 b	11 946 b		4 458		2, 3, 4
4 568			15 968			4 568		2, **4**
			15 696			4 840		2, 3, 4
5 047 b						5 047		**1**, 2, **4**
5 142 b			15 394 vw			5 142		2, **4**
5 368	5 350		15 171			5 367	$^3F_2$	4
5 433	5 417 sh	5 383	15 105 sh,vw			5 433		2
			15 088			5 448		3
5 537						5 537		1
6 483		6 433				6 483	$^3F_3$	**1**, 2
	6 483	6 450	14 036			6 499		2, **3**
6 560	6 543		13 975			6 561		2, **4**
			13 939* vw					
	6 782	6 750	13 736 vw			6 800		2, **3**
6 833	6 814		13 704			6 833		2, **4**
6 998	6 981	6 947	13 538 vw			6 998		2
7 103			13 435			7 102	$^3F_4$	2, **4**
7 134	7 117	7 084	13 402			7 134		2
7 160						7 160		**1**, 2, **4**
7 302			13 233			7 303		2, **4**
	7 326		13 191			7 345		2, **3**, **4**
7 426 b						7 426		**1**, 2, **4**
9 713	9 695	9 663				9 713	$^1G_4$	2
9 731						9 731		**1**, 2, **4**
9 825		9 777				9 825		**1**, 2
10 117						10 117		**1**, 2, **4**
10 256						10 256		**1**, 2, **4**

b: broad, sh: shoulder, w: weak, vw: very weak, [a]: unresolved line, *: uncertain line, [b]: forbidden line. The levels between parenthesis were not introduced in the calculations.

Table 3. Absorption spectrum and excitation at 60 K for $^1D_2$, $^3P_{0,1,2}$ and $^1I_6$ (cm^{-1}).

Absorption			Excitation			Terminal level	$^{2S+1}L_J$	Γ_n
Starting level			Starting level					
$^3H_4(1)$ 0 Γ_3	$^3H_4(2)$ 18 Γ_1	$^3H_4(3)$ 50 Γ_4	$^3H_4(1)$ 0 Γ_3	$^3H_4(2)$ 18 Γ_1	$^3H_4(3)$ 50 Γ_4			
16 403		16 353	16 403		16 353	16 403	$^1D_2$	1
16 413	16 395	16 364	16 412	16 394	16 362	16 413		2
			16 430* b,w					
16 884		16 833	16 886		16 834	16 885		1
	17 065 vw	17 032			17 031	17 082		3
17 215			17 218			17 217		4
20 536		20 485	20 534	20 516[b]	20 484	20 536	$^3P_0$	1
			20 728 w		20 675 w	20 728	$^1I_6$	**1**, 2
				20 728	20 696 w	20 746	$^1I_6$	2, **3**
20 804	20 786		20 801	20 783		20 803	$^1I_6$	2, **4**
			20 830 w			20 830	$^1I_6$	**1**, 2, **4**
21 043	21 025	20 992	21 038	21 020	20 988	21 041	$^3P_1$	2
				21 104		21 122	$^3P_1$	2, **3**, **4**
21 142	21 123		21 136	21 118		21 139	$^3P_1$	2, **4**
	21 150			21 142		21 164	$^1I_6$	2, **3**, **4**
21 677		21 625	21 667	21 617		21 672	$^1I_6$	**1**, 2
	21 812	21 781		21 805	21 771	21 827	$^1I_6$	2, **3**
21 876	21 860 sh		21 868			21 872	$^1I_6$	**1**, 2, **4**
22 107	22 089	22 056	22 103	22 085	22 051	22 105	$^3P_2$	2
22 156			22 147 b			22 152	$^3P_2$	**1**, 2, **4**
22 266* sh,b			22 250 sh					
			22 267 sh			22 267	$^3P_2$	**1**, 2, **4**
22 299			22 293			22 296	$^3P_2$	**1**, 2, **4**

Excitation spectra: $E_{obs.} = 12\,101$ cm^{-1} [$^1D_2(1) \rightarrow {}^3H_6(1)$] for $^1D_2$ and $E_{obs.} = 13\,975$ cm^{-1} [$^3P_0(1) \rightarrow {}^3H_3(3)$] for $^3P_{0,1,2}$ and $^1I_6$. b: broad, sh: shoulder, w: weak, vw: very weak, *: uncertain line, [b]: forbidden line.

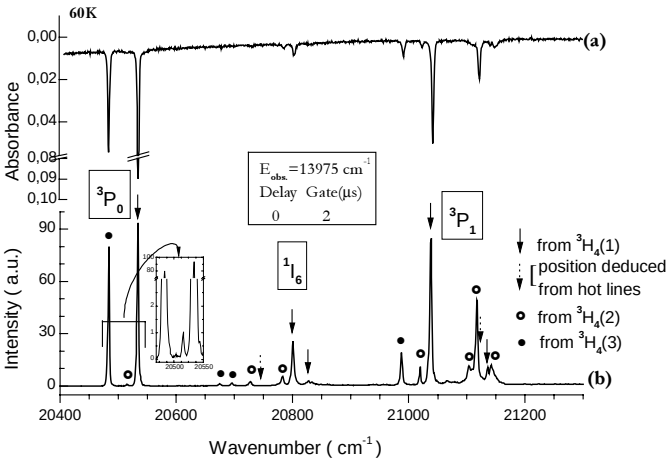

Fig. 11. $^3H_4 \rightarrow {}^3P_0$, $^1I_6$, $^3P_1$ absorption (a) and excitation spectrum (b) at 60 K. The excitation spectrum is obtained by monitoring the $^3P_0 \rightarrow {}^3F_3(3)$ emission at 13 975 cm^{-1} when the excitation wavelength is scanned through the $^3H_4 \rightarrow {}^3P_0$, $^1I_6$, $^3P_1$ absorption spectral region; (o) and (•) indicate absorption from $^3H_4(2)$ and $^3H_4(3)$ respectively. Solid and dotted arrows denote absorption from $^3H_4(1)$ and the position deduced from hot lines (o, •) respectively.

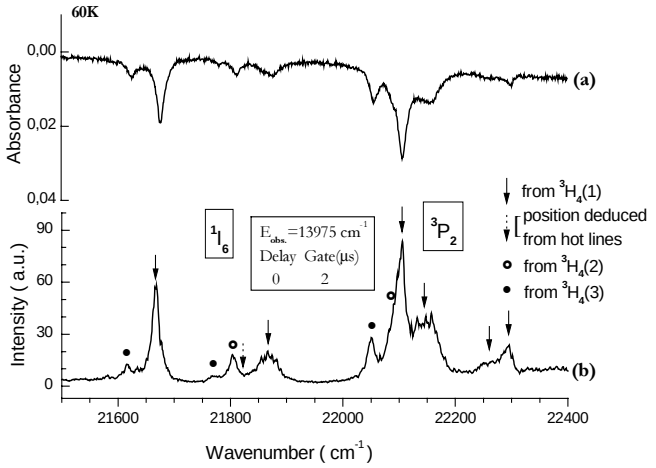

Fig. 12. $^3H_4 \rightarrow {}^1I_6$, $^3P_2$ absorption (a) and excitation spectrum (b) at 60 K. The excitation spectrum is obtained by monitoring the $^3P_0 \rightarrow {}^3F_3(3)$ emission at 13 975 cm^{-1} when the excitation wavelength is scanned through the $^3H_4 \rightarrow {}^1I_6$, $^3P_2$ absorption spectral region. (o, •) Solid and dotted arrows have same meaning as in the Figure 11.

Γ_4), and 11 (Γ_1, Γ_2 or Γ_4). In Tables 2 and 3, the representations which have a larger probability are typed in bold form. For instance, transitions from $^3H_4(1)\Gamma_3$, $^3H_4(2)\Gamma_1$ and $^3P_0\Gamma_1$ to the $^3F_3$ level at 6 833 cm^{-1} are observed, so that the terminal level can be Γ_2 or Γ_4. Since the transition to this level from $^3H_4(3)\Gamma_4$ is not observed, there is a large probability for its representation to be Γ_4 which is written in bold form. The levels of the $^1I_6$ and ^3P_J multiplets in Tables 2 and 3 do not completely agree with the set determined by Malinowski *et al.* [7] from the excitation spectra of upconverted $^3P_0$ emission by pumping the lowest level of $^1G_4$. It is noteworthy that their crystal contained 6 Pr^{3+} sites. There exist also some differences between the energy level set listed in Tables 2 and 3 and the one reported by Gruber *et al.* (Tab. 7 in Ref. [6]). Some levels have different energies, and the assignments of common lines are not always in agreement. Here are some specific points of disagreements.

(a) The authors of reference [6] report that they obtained the emission lines from $^1D_2(2)$ by selective excitation into $^1D_2(2)$ at 16 409 cm^{-1} (their reported value) at 1.6 K (Fig. 9 in Ref. [6]). At that temperature, it seems that they should obtain the emission lines from $^1D_2(1)$ at 16 403 cm^{-1} (their reported value), not from $^1D_2(2)$ at 16 409 cm^{-1}, because relaxation between $^1D_2(1)$ and $^1D_2(2)$ is very fast and rapidly establishes a Boltzman population distribution. If the temperature is higher, then the emission lines from the both $^1D_2(1,2)$ levels should appear. In either case, it is improbable to observe the emission lines from only the $^1D_2(2)$ level. Actually Figure 9 in reference [6] represents the emission lines from the $^1D_2(1)$ level. The first and third lines in that Figure 9 correspond to the $^1D_2(1)\Gamma_3 \rightarrow {}^3H_4(1,3)\Gamma_1$, Γ_4 and the second very weak line corresponds to the forbidden transition $^1D_2(1)\Gamma_1 \rightarrow {}^3H_4(2)\Gamma_1$. Their positions of the energy levels and assignments made on the basis of emission lines from $^1D_2(2)$ instead of $^1D_2(1)$ for the levels of $^3H_4$ and $^3H_5$ multiplets seem to be erroneous. For example, their levels at 533 and 742 cm^{-1} should be 9 cm^{-1} lower and they cannot belong to the Γ_1 representation (Tab. 3, in Ref. [6]), but to Γ_2, Γ_3 or Γ_4.

(b) In reference [6], the spectra are analyzed on the basis that all the allowed transitions should be observed, and the forbidden ones, invisible, which is a probable, but not certain hypothesis. Indeed, we have observed weak lines which are transitions of Pr^{3+} in D_2 and also three very weak forbidden transitions: $^3H_4(2)\Gamma_1 \rightarrow {}^3P_0\Gamma_1$ absorption in the excitation spectrum monitored at 13 975 cm^{-1} corresponding to $^3P_0 \rightarrow {}^3F_3(3)$ and $^1D_2(1)\Gamma_1 \rightarrow {}^3H_6(2)\Gamma_1$, $^3H_6(3)\Gamma_1$ in the emission spectrum. The spectrum in the inset of Figure 11b presents the transition $^3H_4(3,2,1) \rightarrow {}^3P_0$ at 60 K. The very weak line at 20 518 cm^{-1} corresponds to the forbidden transition $^3H_4(2)\Gamma_1 \rightarrow {}^3P_0\Gamma_1$. This suggests that the site symmetry of Pr^{3+} in YAG is not exactly D_2 but might be lower. However forbidden lines cannot have large intensities: for instance, the authors of reference [5] assign the line observed at 20 518 cm^{-1} in the absorption spectrum at 4.2 K to the $^3H_4(2)\Gamma_1 \rightarrow {}^3P_0\Gamma_1$ transition, because this line is separated by 18 cm^{-1} from $^3P_0$ at 20 536 cm^{-1}. It is highly improbable that the relative intensity of the a forbidden transition be as intense as a strong allowed one (Fig. 1 in Ref. [5]).

4 Crystal field analysis

The crystal field analysis was performed firstly by the standard method, within the $4f^2$ configuration only and secondly in the framework of the CIACF (configuration-interaction-assisted-crystal field model). The energy levels were fitted by trial and error after diagonalization of the interaction matrix. The expression of the Hamiltonian [21–25] is given by:

$$
\begin{aligned}
H = & \\
& \sum F^k f_k + \zeta(f) A_{so}(f) + \alpha L(L+1) + \beta G(G_2) + \gamma G(R_7) \\
& + \sum M^k m_k + \sum P^k p_k + \sum B^k_{\mathrm{q}}(f,f) C^k_q(f,f) \\
& + \sum R^k(f,l_1,l_2,l_3) g(f,l_1,l_2,l_3,k) + \zeta(l) A_{so}(l) \\
& + \sum B^k_q(f,l) C^k_q(f,l)
\end{aligned}
$$

f, l, l_1, l_2, l_3 are the orbital moments. The ground configuration is described by seven free-ion parameters: the central field (F^0), electrostatic repulsion (F^k, $k = 2$, 4, 6), spin-orbit ($\zeta(f)$), two-body configuration (α, β, γ), orbit-orbit (M^k), and electrostatically correlated spin- orbit (P^k). γ is ascribed a constant value while the M^k, P^k are constrained by the fixed ratios ($M^2/M^0 = 0.56$; $M^4/M^0 = 0.38$; $P^4/P^2 = 0.75$; $P^6/P^2 = 0.5$ [26]). In addition, the D_2 site symmetry of the A cation in the $A_3B_5O_{12}$ compounds gives rise to 9 crystal field parameters (CFP): B^2_0, B^2_2, B^4_0, B^4_2, B^4_4, B^6_0, B^6_2, B^6_4 and B^6_6. The number of variable parameters in $4f^2$ amounts therefore to 9 free-ion and 9 crystal field parameters, which makes a total of 18. The configuration-interaction-assisted crystal field analysis was described earlier in references [27–31].

Several methods have been utilized to improve crystal field fits: the correlation (two-electron) crystal field model [32–34] has been applied with success for the improvement of the description of singlet states. It presents the advantage of acting on the ground configuration only. Kornienko *et al.* [35] utilize also an effective Hamiltonian working on the states of the ground configuration, with one-electron crystal field parameters depending on the energy of the multiplets. A linear dependence of the crystal field parameters on the energy is convenient for the Ln^{3+} ions.

We have chosen to enlarge the interaction matrix so as to include, in addition to the ground configuration one or several excited configurations and calculate directly the complete interaction. Here, we shall include the $4f6p$ configuration that is, perform the diagonalizations within the $4f^2 + 4f6p$ interaction matrix (dimension $91 + 84 = 175$). The excited $4f6p$ configuration and its interaction with $4f^2$ are defined by the configuration-interaction coulomb integrals $R^k(f, l_1, l_2, l_3)$, a spin-orbit coupling constant

Table 4. Crystal field parameters of Nd^{3+} in YAG: 1 - evaluated by the covalo-electrostatic model for Nd^{3+} [37]; 2 - transposed values for Pr^{3+}; 3 - fitted parameters from reference [6]; 4 - fitted parameters in $4f^2$, this work; 5 - fitted parameters in $4f^2+4f6p$.

	Parameter	B_0^2	B_2^2	B_0^4	B_2^4	B_4^4	B_0^6	B_2^6	B_4^6	B_6^6
1 -	Nd^{3+}	−158	−534	−2 661	−350	1 124	1 365	609	1 727	369
2 -	Pr^{3+}	−170	−574	−2 869	−405	1 212	1 675	747	2 119	453
3 -	Ref. [6]	−391	−233	−3 023	−428	1 268	1 024	335	1 585	7
4 -	$4f^2$	−427	−88	−3 171	−322	1 359	713	243	1 690	195
5 -	$4f^2$	−294	−224	−2 636	−528	1 256	1 543	431	1 951	21
	$+4f6p$	−3 195	−2 436	−19 922	−3 993	9 494				

$\zeta(p)$ and 6 crystal field parameters (f,p): B_0^2, B_2^2, B_0^4, B_2^4, B_4^4. Theoretical values of the gap between both configurations $F^0(f,p) - F^0(f,f)$, of $\zeta(p)$, and of the R^k's are evaluated by Cowan's RCN31 program [36]. One unique variable multiplier X is defined as a phenomenological multiplier of the $R^k(f,l_1,l_2,l_3)$. Actually only the two hybrid integrals $R^k(f,f,f,p)$ (with $k = 2$ and 4) have an efficient action. $B_0^2(f,p)$ and $B_0^4(f,p)$ are individually refined, and it is assumed that the other CFP's of the excited configuration are given by $B_0^k/B_q^k(f,p) = B_0^k/B_0^k(f,f)$. There are therefore three extra parameters in the crystal field analysis involving the excited $4f6p$ configuration: X, $B_0^2(f,p)$, and $B_0^4(f,p)$. The crystal field analysis is performed with starting values of the CFP evaluated by the covalo-electrostatic model in reference [37]. The values for Nd^{3+} are transposed to Pr^{3+} by multiplying by the ratio of radial integrals $\langle r^k\rangle(Pr^{3+})/\langle r^k\rangle(Nd^{3+})$, *i.e.* 1.078, 1.156 and 1.227 for $k = 2$, 4, 6 respectively. The values are listed in Table 4. In Table 4 are also reported the parameters fitted by Gruber *et al.* [6], corresponding to the crystallographic setting 1. They were transformed into setting 3 which is the one utilized by Burdick *et al.* (Ref. [38]). A first diagonalization with the starting parameters listed in Table 4 produces an energy level scheme quite different from the experimental one, with however, a group of three levels at 0, 112 and 158 cm^{-1} well separated from the other six which start 300 cm^{-1} higher. In agreement with the calculation and the assignments of Gruber *et al.*, the three first levels were assigned as Γ_3, Γ_1, and Γ_4 at 0, 18 and 50 cm^{-1} respectively. The subsequent assignments were all compatible with this ordering.

The crystal field analysis was then carried out by introducing at first those levels for which the assignments were uniquely determined, and then by adding progressively those for which there were only two possibilities and by priviledging the most probable representations, at last by filling up with the remaining levels. Two calculations were carried out: firstly in the ground $4f^2$ configuration, and secondly by taking into account the interaction with the excited $4f6p$ configuration. We had to eliminate two weak lines at 544 and 2 629 cm^{-1} because no level in the vicinity, given the possible assignments, was compatible with the calculation.

The four higher levels corresponding to broad and strong absorption lines were left aside at first. The final mean deviation in a $4f^2$ calculation involving the 63 lower levels is equal to 23.8 cm^{-1} and the fitted parameters are listed in Table 5 column 3. Gruber *et al.* [6] obtain a mean deviation equal to 11 cm^{-1} for 52 experimental levels, leaving aside the $^1I_6$ multiplet. The levels assignments of these authors are somewhat different from ours.

Table 6 lists the experimental levels in column 2, the experimentally determined assignments in column 3 and the calculated assignments in column 4. The differences between experimental and calculated energies for the $4f^2$ calculation (63 levels) are reported in column 6. A second calculation based on the same levels with the configuration interaction $4f^2 + 4f6p$ switched on, results in a decrease of the mean deviation down to 13.2 cm^{-1} (column 2 in Tab. 5). The differences between experimental and calculated energies are listed in Table 4, column 5.

The integrated intensity of the four highest absorption lines at 22 105, 22 152, 22 267 (the latter is broad and badly resolved) and 22 296 cm^{-1} (Fig. 12) is reported in Table 7. In that spectral area, the calculation displays five levels, two of which belong to Γ_2 and three to Γ_1 representations. In order to determine the ordering of the levels, and if the two Γ_2 are grouped, we can only rely on a consideration of the lines intensities. We assume that the intensities are directly proportional to the $^3P_2$ content in the wavevector. The wavevectors have similar compositions in both the $4f^2$ and $4f^2 + 4f6p$ calculations, but their ordering is different. The two Γ_2 levels are well separated, one of the them has a leading $^3P_2$ component equal to 67 and 74% while the other has a 18–23 $^3P_2$ content. The level with the highest $^3P_2$ content is therefore identified as the Γ_2 level at 22 105 cm^{-1}. The ordering of the energies is reversed in calculation 2. This reversal is taken into account in Table 7. Among the three remaining Γ_1 levels, one has a 83–85% $^3P_2$ content. We assign it to the second strongest $^3P_2$ component at 22 152 cm^{-1}. The two remaining Γ_1 levels have $^3P_2$ contents equal to 30 and 29%, 50 and 39% in $4f^2$ and $4f^2 + 4f6p$ respectively. They are assigned to the 22 267 and 22 296 cm^{-1} levels. We note that we have to reverse the ordering of the two first Γ_1 levels in both calculations. Actually, two levels which have been classified as $^3P_2$ have also a strong $^1I_6$ content. Two more calculations (3 and 4) were run using the complete set of 67 levels, in $4f^2 + 4f6p$ and $4f^2$ respectively (columns 7 and 8 in Tab. 6). We note that calculation 3 is the only one where the ordering of all the calculated $^3P_2$ levels are in agreement with the experimental ones. The mean deviations over the whole set of 67 levels are then equal to 21.7 and 28.5 cm^{-1} (with and without CI resp.). CI improves

Table 5. Free ion and crystal field parameters (cm^{-1}) of Pr^{3+} in YAG without and with configuration interaction. X is the fitted multiplier of the R^k's. The following values (all in cm^{-1}) were held constant: $\gamma = 1\,515$ cm^{-1}, $F^0(f,p) - F^0(f,f) = 124\,343$ cm^{-1}, $\zeta(p) = 3\,800$ cm^{-1}, $R^2(f,p,f,p) = 11\,576$, $R^2(f,f,p,p) = 3\,249$, $R^4(f,f,p,p) = 2\,973$, $R^2(f,f,f,p) = -4\,886$, $R^4(f,f,f,p) = -2\,968$. The standard deviations are between parentheses.

levels	63 Levels (without $^3P_2$)		67 Levels (with $^3P_2$)	
	(1)	(2)	(3)	(4)
	$4f^2 + 4f6p$	$4f^2$	$4f^2 + 4f6p$	$4f^2$
Parameters				
$F^0(f,f,f,f)$	10 424 (32)	10 173 (5)	10 408 (39)	10 167 (4)
$F^2(f,f,f,f)$	67 239 (45)	67 044 (65)	67 179 (58)	67 007 (59)
$F^4(f,f,f,f)$	49 121 (127)	48 798 (217)	49 197 (176)	49 014 (193)
$F^6(f,f,f,f)$	32 530 (104)	31 969 (145)	32 511 (117)	32 120 (130)
α	22.1 (0.4)	22.59 (0.56)	22.63 (0.46)	22.83 (0.52)
β	−708 (22)	−642 (35)	−730 (32)	−668 (36)
M^0	1.58 (0.43)	0	1.61 (0.56)	0
P^2	199 (101)	296 (190)	529 (100)	567 (122)
$\zeta(f)$	739.7 (3.3)	730.3 (5.8)	730.1 (4.0)	722.6 (4.6)
$B^2_0(f,f)$	−288 (23)	−420 (26)	−292 (34)	−427 (26)
$B^2_2(f,f)$	−245 (56)	−86 (33)	−226 (66)	−88 (32)
$B^4_0(f,f)$	−2 671 (70)	−3 231 (64)	−2 620 (95)	−3 171 (60)
$B^4_2(f,f)$	−591 (93)	−301 (57)	−525 (107)	−322 (60)
$B^4_4(f,f)$	1 245 (40)	1 379 45)	1 252 (71)	1 359 (46)
$B^6_0(f,f)$	1 537 (108)	795 (95)	1 506 (156)	713 (90)
$B^6_2(f,f)$	555 (106)	318 (73)	424 (121)	243 (69)
$B^6_4(f,f)$	2 010 (67)	1 728 (64)	1 957 (74)	1 690 (66)
$B^6_6(f,f)$	124 (92)	191 (86)	32 (116)	195 (90)
$X^2 = X^4$	1.571		1.440	
$B^2_0(f,p)$	−2 395		−3 179	
$B^4_0(f,p)$	−20 600		−19 995	
σ	13.2	23.8	21.8	28.5
n	21	17	21	17
N	63	63	67	67
SD	16.2	27.9	26.3	33.0

N: Number of the experimental levels introduced in the fit. n: Number of the parameters which are allowed to vary freely. SD = Standard deviation: $[\Sigma_{i=1,n}(E_{i\text{exp.}} - E_{i\text{calc.}})^2/(N-n)]^{1/2}$. σ: Un-barycentered mean deviation.

the agreement experimental/calculated to a certain extent (24% and 20% for the mean and standard deviations respectively). If the mean deviation is evaluated separately for the four $^3P_2$ levels, and for the 63 other levels, the results are: 57 and 64 cm^{-1} for the $^3P_2$ levels, 17.1 and 24.5 cm^{-1} for the other 63 levels, in the calculations with and without CI. It is noteworthy that when only 63 levels are introduced into the refinement process, the $^3P_2$ levels which are out of control drift up towards high energies and their mean deviations are equal to 108 and 98 cm^{-1}, in calculations 1 and 2, with and without configuration interaction respectively (Tab. 6). However, as already mentioned, the mean deviation of the 63 levels is improved and amounts to 13.2 cm^{-1}.

In Table 6 column 4 are indicated the levels representations in the four calculations. For 57 levels, the representations in the four calculations are identical and belong to the allowed experimental set indicated in column 3. They are considered as correct. There were only 21 experimentally determined assignments. At the light of the calculations, there are now 57 fully identified levels. Five Γ_2 levels do not belong to the set of "most probable" assignments written in bold form in Table 6, whereas 23 levels do.

For 10 remaining levels, the representations are not the same in the four calculations. This occurs when adjacent energy levels are very close to one another, with energy differences of the order of 10 to 20 cm^{-1}. For instance it is not possible to state which of the three $^3H_4$ levels at 526, 544 and 576 cm^{-1} is Γ_2, Γ_3 or Γ_4. Actually, we believe that calculation 3 is the most reliable and Γ_4, Γ_3, Γ_2 is the correct ordering.

Figure 13 plots the mean deviation of the crystal field analysis in the $4f^2$ and the $4f^2 + 4f6p$ analysis for the six praseodymium doped compounds investigated by us up to now: the solid curve represents the analysis in $4f^2$ and the dotted curve that in $4f^2 + 4f6p$. The mean deviation in $4f^2$ seems to increases for crystal field strengths lower than 500 cm^{-1}, reach a maximum and eventually

Table 6. Experimental energy levels, experimentally determined and calculated symmetry assignments and differences between experimental and calculated energies for $4f6p$ and $4f^2$ calculations.

$^{2S+}L_J$	$E_{\mathrm{exp.}}(\mathrm{cm}^{-1})$	$\Gamma_{n\,\mathrm{exp}}$	$\Gamma_{n\mathrm{Cal.}}$	63 Exp. Levels		67 Exp. Levels	
			(1) (2) (3) (4)	(1) $4f^2+4f6p$	(2) $4f^2$	(3) $4f^2+4f6p$	(4) $4f^2$
				ΔE			
$^3H_4$	0	3	3	8	−15	2	33
	18	1	1	14	29	16	−16
	50	4	4	4	−5	−4	−18
	(555)	2, 3, 4	1	/	/	/	/
	526	2, 3, 4	3 2 4 2	−4	−7	−8	1
	544	2, 3, 4	4 3 3 4	−4	7	−2	5
	576	2, 3, 4	2 4 2 3	10	22	19	31
	730	2, 3, 4	2	−14	−18	−9	−16
	/	/	1	/	/	/	/
σ				9.3	16.9	9.6	20.4
$^3H_5$	2 279	3, 4	4 3 4 3	0	8	−1	8
	2 293	3, 4	3 4 3 4	9	11	10	17
	/	/	2	/	/	/	/
	/	/	1	/	/	/	/
	2 398	2, 3, 4	2	−7	0	−3	−1
	(2 629)	2, 3, 4	1	/	/	/	/
	2 574	2, 3, 4	3 4 3 3	−29	−28	−21	−17
	2 583	3, 4	4 3 4 4	−25	−20	−35	−24
	2 618	2, 3, 4	2	−11	−20	−11	−14
	2 839	2, 3, 4	4	25	22	25	25
	2 861	2, 3, 4	3	4	8	13	11
σ				17.2	17.0	18.3	16.4
$^3H_6$	4 303	4	4	−10	−27	−19	−29
	4 316	1	1	−4	−13	−3	−12
	4 340	3	3	−9	−11	−17	−17
	4 358	1, 4	1	15	15	4	9
	4 409	2, **3**, **4**	2	1	21	−7	17
	4 458	2, 3, 4	3	−22	−43	−24	−44
	4 568	2, **4**	4	13	8	13	1
	/	/	3 3 1 3				
	/	/	1 1 3 1				
	4 840	2, 3, 4	4 4 4 2	23	32	36	−12
	/	/	2 2 2 4				
	5 047	**1**, 2, **4**	1	11	19	7	17
	5 142	2, **4**	2	1	30	10	32
σ				13.1	24.3	16.8	22.4
$^3F_2$	5 367	4	4	−9	−34	−28	−39
	5 448	3	3	5	−30	9	−27
	5 433	2	2	−11	22	−23	16
	/	/	1	/	/	/	/
	5 537	1	1	−4	15	−1	20
σ				7.8	26.3	18.7	27.0
$^3F_3$	6 483	**1**, 2	1	2	2	−3	−2
	6 499	2, **3**	3	5	27	−6	19
	6 561	2, **4**	4	12	0	25	2
	6 800	2, **3**	3	14	17	10	21
	6 833	2, **4**	4 2 4 4	−6	−3	8	8
	/	/	2 4 2 2	/	/	/	/
	6 998	2	2	12	−25	−6	−14
σ				9.6	16.6	12.0	13.4

Table 6. *Continued.*

$^{2S+}L_J$	$E_{\text{exp.}}(\text{cm}^{-1})$	$\Gamma_{n\,\text{exp}}$	$\Gamma_{n\text{Cal.}}$	63 Exp. Levels		67 Exp. Levels	
$^3F_4$	7 102	2, **4**	4	16	58	27	65
	/	/	3	/	/	/	/
	7 160	**1**, 2, **4**	1	17	39	25	35
	7 134	2	2	−13	−49	−9	−46
	/	/	1	/	/	/	/
	/	/	2 4 2 4	/	/	/	/
	7 303	2, **4**	4 2 4 2	−9	−21	−10	−25
	7 345	2, **3**, **4**	3	−2	−37	12	−37
	7 426	**1**, 2, **4**	1	−17	−36	−12	−34
σ				13.5	41.6	17.4	42.3
$^1G_4$	9 713	2	2	25	28	34	25
	/	/	4	/	/	/	/
	9 731	**1**, 2, **4**	1	−7	40	0	34
	/	/	3	/	/	/	/
	9 825	**1**, 2	1	−28	−19	−9	−11
	10 117	**1**, 2, **4**	4	8	0	−3	−1
	10 256	**1**, 2, **4**	2	8	−26	9	−25
	/	/	3	/	/	/	/
	/	/	1	/	/	/	/
σ				17.8	26.2	16.3	22.5
$^1D_2$	16 413	2	2	9	9	11	12
	16 403	1	1	−22	−38	−5	−39
	16 885	1	1	−13	−4	−20	−11
	17 082	3	3	15	−5	24	−1
	17 217	4	4	17	42	36	45
σ				15.8	25.8	22	27.6
$^3P_0$	20 356	1	1	1	1	−32	−14
$^1I_6$	20 728	**1**, 2	1	−2	−1	1	2
$^1I_6$	20 746	2, **3**	3	−9	−12	−6	−6
$^1I_6$	20 803	2, **4**	4	2	−9	2	−14
$^1I_6$	20 830	**1**, 2, **4**	2	-3	-27	-5	-28
$^3P_1$	21 041	2	2	7	−4	21	21
$^3P_1$	21 122	2, **3**, **4**	4	-12	-14	3	11
$^1I_6$	21 139	2, **4**	2	0	−14	9	9
$^1I_6$	/	/	1	/	/	/	/
$^3P_1$	21 164	2, **3**, **4**	3	−15	−18	6	7
$^1I_6$	21 672	**1**, 2	1	21	30	41	46
$^1I_6$	21 827	2, **3**	3	21	31	35	50
$^1I_6$	21 872	**1**, 2, **4**	4	−16	-4	10	11
$^1I_6$	/	/	4	/	/	/	/
$^1I_6$	/	/	3	/	/	/	/
$^3P_2$+$^1I_6$	22 105	2	2	(0)	(−60)	58	38
$^1I_6$	/	/	2	/	/	/	/
$^3P_2$	22 152	**1**, 2, **4**	1	(−140)	(−152)	−63	−91
$^3P_2$+$^1I_6$	22 267	**1**, 2, **4**	1	(−1)	(37)	24	75
$^3P_2$+$^1I_6$	22 296	**1**, 2, **4**	1	(−165)	(−104)	−72	−34
$^3P_2$+$^1I_6$	/	/	4	/	/	/	/
$^3P_2$+$^1I_6$	/	/	3	/	/	/	/
$\sigma(^3P_1)$				11.8	13.4	12.7	14.3
$\sigma(^1I_6)$				12.4	20.2	19.9	27.0
$\sigma(^3P_2)$				(108)	(98)	57	64

Table 7. Experimental and calculated energy levels (in cm^{-1}), integrated area (in Å) of the absorption transition from $^3H_4$ and leading components of the "$^3P_2$" levels.

Calculation			(1) fp 63			(2) f^2 63			(3) fp 67			(4) f^2 67		
E_{exp}	I	Γ	E_{calc}	$\vert\ \rangle$		E_{calc}	$\vert\ \rangle$		E_{calc}	$\vert\ \rangle$		E_{calc}	$\vert\ \rangle$	
				$^3P_2$	$^1I_6$		$^3P_2$	$^1I_6$		$^3P_2$	$^1I_6$		$^3P_2$	$^1I_6$
22 105	0.2	2	22 105	0.67	0.26	22 165	0.74	0.19	22 047	0.87	0.06	22 067	0.58	0.37
		2	22 180	0.23	0.72	22 101	0.18	0.73	22 138	0.05	0.92	22 109	0.35	0.61
22 152	0.18	1	22 292	0.85	0.07	22 304	0.83	0.06	22 215	0.85	0.04	22 243	0.79	0.13
22 267	0.03	1	22 268	0.29	0.50	22 230	0.30	0.65	22 243	0.35	0.42	22 192	0.34	0.46
22 296	0.03	1	22 461	0.39	0.32	22 400	0.50	0.19	22 368	0.29	0.48	22 330	0.41	0.32

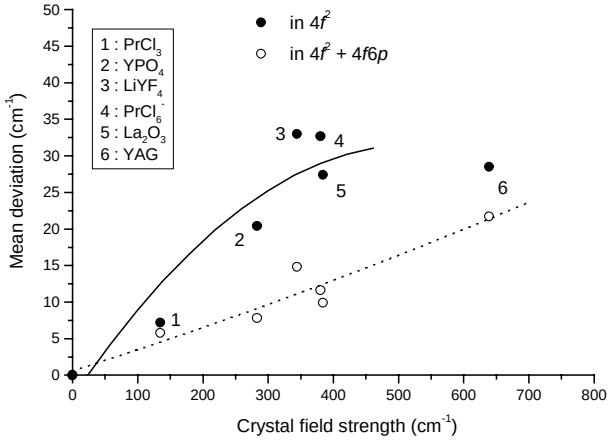

Fig. 13. Mean deviation of the crystal field analysis *versus* crystal field strength in Pr^{3+} compounds, with and without configuration interaction.

decrease for YAG:Pr^{3+} ($E = 639$ cm^{-1}), which is difficult to understand. The mean deviation utilizing $4f^2 + 4f6p$ increases steadily. Figure 13 shows that the improvements of the energy level fits were more important in the cases formerly studied of $LiYF_4$, YPO_4, $PrCl_6^-$ and La_2O_3. This might suggest that the configuration assisted crystal field method becomes less efficient for strong crystal fields. However it is not true for Cs_2UBr_6 and $Cs_2Zr(U)Br_6$ ($U^{4+} = 4f^2$) [39]. The crystal field strength of these compounds is equal to 1 363 cm^{-1}, a far larger value than considered here and yet the improvement due to CI amounts to 80%. Taking into account the small number of investigated compounds it is difficult to state whether YAG:Pr^{3+} behaves abnormally or not. One point singularizes YAG:Pr with respect to other compounds: it is the strong mixing of $^3P_2$ with $^1I_6$. This mixing explains the strong intensity of some of the $^3H_4 \rightarrow {}^1I_6$ absorption lines, for instance the $^3H_4(1) \rightarrow {}^1I_6(7)$ transition at 21 672 cm^{-1}. It has a large $^3P_2$ content so that what is observed is the $^3H_4 \rightarrow {}^3P_2$ component of the transition. For a large number of Pr^{3+} compounds, the majority of the $^1I_6$ levels are invisible and two-photon experiments have to be carried out to complete the determination of the energy level scheme. The mixing of $^3P_2$ with $^1I_6$ levels is not direct. It occurs through two interactions: (a) a $^3P_2$–$^1D_2$ spin-orbit interaction which is nearly constant whatever the compound, and (b) a strong $^1D_2$–$^1I_6$ host dependent crystal-field interaction produced by large $k = 6$ order parameters. Therefore the $^3H_4 \rightarrow {}^1I_6$ transitions should be strong for all the compounds having large $k = 6$ CFP's. It is not the case, however for $YPO_4:Pr^{3+}$ for which most of the $^3H_4 \rightarrow {}^1I_6$ transitions are invisible and yet $B_0^6(f, f) = -1\,379$ cm^{-1}. We can infer, however that the conjunction of large CFP's with k of all orders favor the $^3P_2$–$^1I_6$ mixing.

A logical step would be to allow for YAG:Pr^{3+} the $4f^2/4f5d$ interaction as well as $4f^2/4f6p$. For $YPO_4:Pr^3$, this action resulted in a further decrease of the mean experimental/calculated deviation. The progression was $20.4 \rightarrow 18.7 \rightarrow 7.8 \rightarrow 4.6$ cm^{-1} in $4f^2$, $4f^2 + 4f5d$, $4f^2 + 4f6p$, $4f^2 + 4f6p + 4f5d$, respectively. For YAG:Pr^{3+}, the result is completely different. The point charge model predicts that the only non-vanishing odd crystal field parameters are S_2^3 and S_4^5. Two bands ascribed to $4f^2 \rightarrow 4f5d$ transitions occur in the absorption spectrum at 34 700 and 42 000 cm^{-1}. S_2^3 and S_4^5 values equal to $-3\,500$ and 9 000 cm^{-1} respectively reproduce fairly well the experimental splitting. However, if these values are introduced into the interaction matrix, the lower $^1I_6$ levels are strongly disturbed and impossible to fit. The effect of the $4f5d$ configuration on all the 67 levels is such that the change of the fitted $4f/4f$ crystal field parameters penalizes the $^1I_6$ set. At this step, we cannot interpret this effect. It is probable that another perturbating configuration which we have not yet considered, is involved. The test of an interaction $4f^2/4f5f$ was unsuccessful. In these conditions, it seems pointless to regard a theoretical evaluation of the intensities as very meaningful. Whereas the calculation of $4f^{n-1}5d \rightarrow 4f^n$ intensities are allowed *via* the $\langle f|r|d\rangle$ intensity matrix elements [41–43], the direct calculation of $4f \rightarrow 4f$ intensities requires a prelimary determination of the small admixture of $5d$ states into the $4f$ wavefunctions, prior to evaluating the intensities [40]. A complete study of the $4f \rightarrow 4f$ transitions intensities

is beyond the scope of the present work. What was however done was a diagonalization with very small S_2^3 and S_4^5 parameters, followed by a calculation of the absorption intensities for the highest lines of the spectrum. The intensity of the lines at 22 047, 22 138 22 215, 22 243 and 22 368 cm^{-1} were found proportional to 24, 2, 20, 5, and 7 which compares favorably with the experimental values (Tab. 7) and confirms the empirical considerations based on the leading components of the "$^3P_2$" levels. Less satisfying however is the occurrence of a strong absorption line calculated with a strength equal to 19 at 22 490 cm^{-1}; it is invisible in the absorption spectrum. Therefore, if the $4f^2 + 4f6p$ configuration interaction which is considered in this work, is one step towards the solution, it does not represent the complete solution.

5 Conclusion

It has been recognized that the interpretation of the optical spectra of Pr^{3+} doped $Y_3Al_5O_{12}$ is complicated by various phenomena which are line broadening due to phonon effects [44], satellite structure, inhomogeneous broadening. Non stoichiometric defects have also been suspected. In this context, we felt that another contribution, utilizing a different synthesis technique, and a crystal field analysis including full configuration interaction would be useful. We present therefore a new experimental optical investigation of Pr^{3+} doped $Y_3Al_5O_{12}$ (YAG) on sintered powder samples with several Pr^{3+} concentrations and at different temperatures. The optical spectra of the translucent sample with the lowest concentration (0.07 at.%) are those of Pr^{3+} in the D_2 site of Y^{3+} without any additional lines produced by other sites. This fact seems to refute a former statement following which up to 9% of lanthanide ions can be normally present in the octahedral a sites of pure YAG. A microprobe analysis of our translucent ceramic sample reveals a Y^{3+} deficiency and a Al^{3+} excess with respect to the theoretical composition, a fact which seems to support that there is no structural inversion between "c" and "a" sites of the compound.

For increasing concentrations, satellite lines are observed in the vicinity of all the absorption and emission lines. The intensity of the satellites which are observed beside the $^3H_4(1) \rightarrow {}^3P_0$ absorption line increases quadratically with the dopant concentration proving that they are due to the approach of other Pr^{3+} ions, in larger numbers than a statistic evaluation predicts.

The energy levels of the $4f^2$ configuration of Pr^{3+} were determined by absorption and site selective excitation. Three weak forbidden lines have been observed, which seems to indicate that the symmetry at the Pr^{3+} site is lower than D_2.

69 out of the 91 crystal field levels of Pr^{3+} in YAG have been determined and 67 have been utilized for a crystal field analysis in $4f^2$ and in the enlarged matrix $4f^2 + 4f6p$. The $^3P_2$ levels are the less well fitted and and are strongly mixed with $^1I_6$. The global mean deviation experimental/calculated energy levels is equal to 28.5 and 21.8 cm^{-1} in $4f^2$ and $4f^2 + 4f6p$ respectively. The improvement due to configuration interaction is much less pronounced than in former analyses on Pr^{3+} compounds. The fit in $4f^2 + 4f6p$ ensures however a correct ordering of the experimental levels with respect to their irreducible representations. The behaviour of the $^3P_2$ levels limits the improvement in the CI analysis: the mean deviation for $^3P_2$ levels amounts to 57 cm^{-1} whereas it is only 17 cm^{-1} for the 63 lower levels. When the $^3P_2$ levels are disregarded, and the fit is based on these 63 lower levels only, the mean deviation falls down to 13.2 cm^{-1}. The $^3P_2$–$^1I_6$ mixing is connected with the presence of large crystal field parameters, especially the $k = 6$ order ones and one question which arises concerns the reason why some compounds should have such large parameters, larger than for simple oxides for instance. In a previous work on the derivation of semi-empirical values of CFP's from the structure, the ionic charges, the theoretical atomic wavefunctions, [37], we noted that the B_q^6 parameters of the oxide compounds with Al^{3+} ions as second neighbours were "abnormally" large. This was verified for $NdAlO_3$, $YAlO_3$:Nd^{3+}, $Ca_{0.8}Mg_{0.2}Al_{11.8}O_{19}Nd_{0.2}$ and $Y_3Al_5O_{12}$:Nd^{3+}.

The authors are indebted to Dr. Eric Leroy, Laboratoire de Chimie Métallurgique, UPR 209 at Thiais for the microprobe analysis of the 0.07% doped sample.

References

1. A.A. Kaminskii, *Laser Crystals* (Springer, New York, 1981).
2. A. Rémilleux, thèse, Lyon-I, 1995.
3. F.N. Hooge, J. Chem. Phys. **45**, 4504 (1966).
4. J.T. Gourley, Phys. Rev. **5**, 22 (1972).
5. E. Antic-Fidancev, M. Lemaître-Blaise, P. Caro, Inorg. Chim. Acta **139**, 281 (1987).
6. J.B. Gruber, M.E. Hills, R.M. MacFarlane, C.A. Morrison, G.A. Turner, Chem. Phys. **134**, 241 (1989).
7. M. Malinowski, M.F. Joubert, B. Jacquier, Phys. Rev. B **50**, 12367 (1994).
8. O.L. Malta, E. Antic-Fidancev, M. Lemaître-Blaise, J. Dexpert-Ghys, B. Piriou, Chem. Phys. Lett. **129**, 557 (1986).
9. V.M. Goldschmidt, T. Barth, G. Lunde, W.H. Zachariasen, *Pt. VII Skrifter Norske Videnskaps-Akad*, Oslo I. Mat.-Naturv. Kl., No. 2, 1926.
10. S.J. Schneider, R.S. Roth, J.L. Waring, J. Res. Nat. Bur. Stand. A **65**, 345 (1961).
11. V. Lupei, A. Lupei, C. Tiseanu, S. Georgescu, C. Stoicescu, P.M. Nanau, Phys. Rev. B **51**, 8 (1995).
12. C. Tiseanu, A. Lupei, V. Lupei, J. Phys. Cond. Matt. **7**, 8477 (1995).
13. O. Guillot-Noël, V. Mehta, B. Viana, D. Gourier, M. Boukhris, S. Jandl, Phys. Rev. B **61**, 15338 (2000).
14. Y. Rabinovitch, D. Tétard, M. Pham-Thi, M. Faucher, unpublished.
15. F. Euler, J.A. Bruce, Acta Cryst. **19**, 971 (1965).
16. S. Geller, Zeit. Kristall. **125**, 1 (1967).

17. B. Piriou, H. Rager, H. Schneider, J. Eur. Ceram. Soc. **16**, 195 (1996).
18. O. Guillot-Noël, B. Viana, B. Bellamy, D. Gourier, G.B. Zogo-Mboulou, S. Jandl, Opt. Mat. **13**, 427 (2000).
19. M. Gaczynski, M. Blazej, W.S. Strek, Mater. Chem. Phys. **31**, 175 (1992).
20. M. Malinowski, P. Szczepanski, W. Wolinski, R. Wolski, Z. Fukacz, J. Phys. Cond. Matt. **5**, 6469 (1993).
21. B.R. Judd, *Operator techniques in Atomic Spectroscopy* (Princeton University Press, 1998).
22. B.G. Wybourne, *Spectroscopic properties of Rare Earths* (Interscience Publishers, John Wiley, New York, 1965).
23. B.R. Judd, Phys. Rev. **141**, 4 (1966).
24. B.R. Judd, H.M. Crosswhite, H. Crosswhite, Phys. Rev. **169**, 130 (1968).
25. K. Rajnak, B.G. Wybourne, Phys. Rev. **132**, 280 (1963).
26. H.M. Crosswhite, H. Crosswhite, J. Opt. Soc. Am. B **1**, 246 (1984).
27. M. Faucher, D.J. Kooy, Sol. State Comm. **102**, 663 (1997).
28. M. Faucher, O.K. Moune, Phys. Rev. A **55**, 4150 (1997).
29. O.K. Moune, M.D. Faucher, C.K. Jayasankar, A.M. Lejus, J. Lumin. **85**, 59 (1999).
30. O.K. Moune, M.D. Faucher, N. Edelstein, J. Lumin. **96**, 51 (2002).
31. P.A. Tanner, C.S.K. Mak, M.D. Faucher, J. Chem. Phys. **114**, 10860 (2001).
32. C.L. Li, M.F. Reid, Phys. Rev. B **42**, 1903 (1990).
33. J.R. Quagliano, G.W. Burdick, D.P. Glover-Fischer, F.S. Richardson, Chem. Phys. **201**, 321 (1995).
34. B.R. Judd, in *Group Theoretical Methods in Physics*, Vol. 79 of Lecture Notes in Physics, edited by P. Kramer, A. Rieckers (Springer-Verlag, Berlin, 1978), p. 417.
35. A.A. Kornienko, E.B. Dunina, J. Exp. Theor. Phys. **89**, 1130 (1999).
36. R.D. Cowan, Computer Program RCN31 (September 1981).
37. M. Faucher, D. Garcia, O.K. Moune, J. Lumin. **51**, 341 (1992).
38. G.W. Burdick, C.K. Jayasankar, F.S. Richardson, M.F. Reid, Phys. Rev. B **50**, 16309 (1994).
39. M.D. Faucher, O.K. Moune, D. Garcia, P. Tanner, Phys. Rev. B **53**, 9501 (1996).
40. D. Garcia, M. Faucher, J. Alloys Comp. **180**, 239 (1992).
41. M.F. Reid, Phys. Rev. B **62**, 14744 (2000).
42. M. Laroche, J.-L. Doualan, S. Girard, J. Margerie, R. Moncorgé, J. Opt. Soc. Am. B **17**, 1291 (2000).
43. M. Laroche, S. Girard, J. Margerie, R. Moncorgé, M. Bettinelli, E. Cavalli, J. Phys. Cond. Matt. 13, 765 (2001).
44. A. Lupei, Opt. Mat. **16**, 153 (2001).